SLAC-PUB-17139

A Method To Generate A Pulse Train Of Few-Cycle Coherent Radiation

Bryant Garcia,[1,*] Erik Hemsing,[1] Tor Raubenheimer,[1]
Lawrence T. Campbell,[2,3] and Brian W. J. McNeil[2]

[1]*SLAC National Accelerator Laboratory, Menlo Park, California 94025, USA*

[2]*SUPA, Department of Physics, University of Strathclyde, Glasgow G4 0NG, UK*

[3]*ASTeC, STFC Daresbury Laboratory and Cockroft Institute, Warrington WA4 4AD, UK*

(Dated: July 18, 2017)

Abstract

We develop a method to generate a long pulse train of few-cycle coherent radiation by modulating an electron beam with a high power laser. The large energy modulation disperses the beam in a radiating undulator and leads to the production of phase-locked few-cycle coherent radiation pulses. These pulses are produced at a high harmonic of the modulating laser, and are longitudinally separated by the modulating laser wavelength. We discuss an analytical model for this scheme and investigate the temporal and spectral properties of this radiation. This model is compared with numerical simulation results using the unaveraged code Puffin. We examine various harmful effects and how they might be avoided, as well as a possible experimental realization of this scheme.

* bryantg@stanford.edu

This material is based upon work supported by the U.S. Department of Energy, Office of Science, under Contract No. DE-AC02-76SF00515.

I. INTRODUCTION

There has been a long history of using lasers to manipulate relativistic electron beams to produce tailored radiation pulses [1] [2]. These methods may seek to produce high harmonic upconversion as in the Coherent Harmonic Generation (CHG) [3] or Echo-Enabled Harmonic Generation [4] schemes, which may be used to seed Free-Electron Lasers (FELs) [5] [6] [7] [8] [9]. Laser manipulations may also target short pulse length, as can be achieved by so-called femtoslicing in synchrotron sources [10] [11] or by interaction with a few-cycle laser pulse to produce an attosecond scale FEL pulse [12]. One can also endeavor to produce pulse trains of radiation with a fixed phase relationship, either by use of delay stages in an FEL [13], by modulating the electron beam to produce sidebands around the FEL resonant wavelength [14], or through seeding via a pulse train from High Harmonic Generation (HHG) techniques [15].

Some of these methods are well suited to merely producing coherent radiation, while others must cautiously avoid spoiling the performance of an FEL interaction. Methods of generating short pulses can also require very precise laser timing control or advanced laser systems. Here we introduce a simple but potentially robust method to produce a train of mode-locked, few-cycle, high harmonic coherent radiation pulses using only a powerful modulation laser, one modulating undulator, and a short radiating undulator. In this paper, we refer to the radiation produced by individual coherently radiating regions of the electron beam as 'pulses', while the assemblage of all such regions over the entire electron beam is referred to as a 'pulse train'. We note that a similar situation utilizing extremely large energy modulations was considered in [16], although the analytical formalism in this paper differs considerably from our own and the emphasis is on high harmonic upconversion, rather than the dispersion-controlled pulse duration.

The fundamental beamline components necessary for the scheme are shown in Fig. 1, which shows schematically the production of the few-cycle radiation pulse train. First, a relativistic electron beam copropagates with a high power laser of wavelength λ_L in a modulating undulator (U1, tuned to λ_L). The resonant interaction between the laser and electron beam imprints a roughly sinusoidal energy modulation on the beam, and in our case this modulation amplitude can be up to several percent of the total beam energy. The beam may then optionally be partially 'pre-bunched' by a small magnetic chicane (C1), in

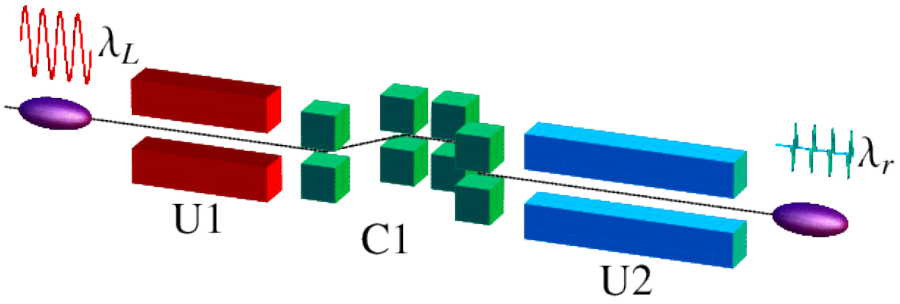

FIG. 1. A schematic illustration of the short pulse train generation scheme. A long-wavelength laser λ_L modulates the electron beam in the first undulator (U1). This beam may then be optionally pre-compressed by a small four-dipole magnetic chicane (C1), before radiating in another undulator (U2) tuned to a high harmonic of the seed laser. The result is a train of few-cycle radiation pulses at the upconverted wavelength λ_r.

order to decrease the need for a long undulator. Next, the modulated electron beam enters a radiating undulator (U2) tuned to a resonant wavelength λ_r, which is chosen to be some harmonic of the modulating laser wavelength: $\lambda_L = h\lambda_r$, for integer h. This undulator is characterized by the longitudinal dispersion transport matrix element $R_{56} = 2N_u\lambda_r$, where N_u is the number of periods in the undulator. We can write this transport element as a function of distance along the undulator z, noting that for an undulator with period λ_u we have the relation $N_u = z/\lambda_u$.

We examine the electron beam in the comoving frame described by longitudinal coordinate $s = z - \bar{\beta}ct$, where $\bar{\beta}$ is the average normalized electron velocity. In this frame as the electron beam traverses this undulator the initial density modulation will be converted into a density modulation, and eventually the beam will over-disperse, as shown in Fig. 2. In this comoving frame, an electron with relative energy deviation $\delta\gamma/\gamma$ will move longitudinally with respect to the reference electron at a rate,

$$\frac{ds}{dz} = \frac{dR_{56}}{dz}\frac{\delta\gamma}{\gamma} = 2\frac{\lambda_r}{\lambda_u}\frac{\delta\gamma}{\gamma}$$

Meanwhile, the electrons are also radiating at the resonant undulator wavelength λ_r. If a localized region of electrons become confined through this compression to a region smaller

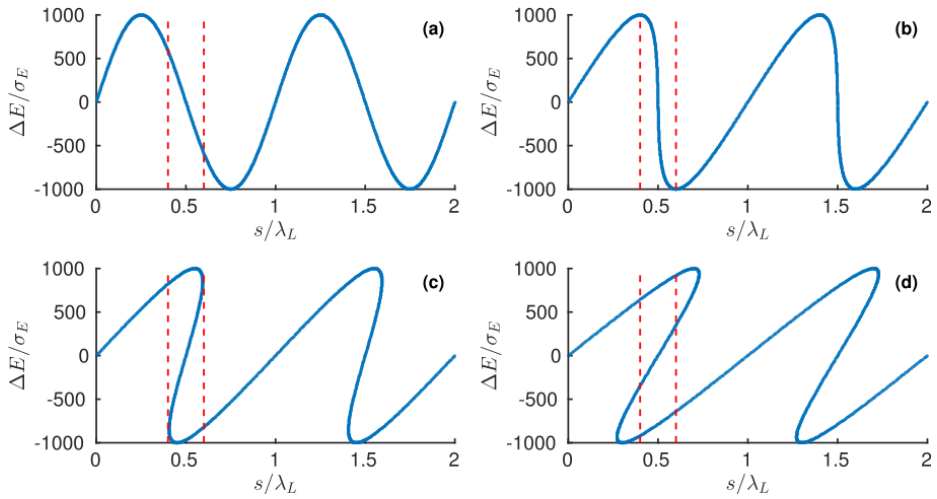

FIG. 2. An illustration of the longitudinal phase space dynamics involved in the generation of short pulses. The red vertical lines correspond to a width of 0.2 λ_L, corresponding to a harmonic upconversion factor $h = 5$. In panel (a) we see the beam initially modulated by 10^3 times the energy spread σ_E. In panel (b) the beam has dispersed into the coherent radiation regime, and it leaves this regime at panel (c). After further dispersion, the beam is as in panel (d), and no longer efficiently radiates coherently.

than λ_r, the emission of radiation will be coherent, corresponding to panels b) and c) of Fig. 2. The longitudinal distance L_p spent in this region thus defines the duration of coherent emission, and can be found simply by dividing the distance an the electron travels during this coherent emission (λ_r) by its relative velocity (ds/dz),

$$L_p \approx \frac{\lambda_r}{\frac{ds}{dz}} = \frac{\lambda_u}{2\delta\gamma/\gamma}$$

The number of coherent radiation cycles can thus be estimated to be $N_{\text{cyc}} \approx \frac{1}{2\delta\gamma/\gamma}$, dependent only on the modulation amplitude. Intuitively, it is easy to understand that the larger the relative energy deviation is, the quicker the electrons disperse longitudinally inside the radiating undulator, leading to a shorter coherent pulse. Indeed, for modulation amplitudes on the order of a few percent, one can achieve few-cycle pulses.

Furthermore, as is clear from Fig. 2, the electron beam will in general be much longer than the modulating laser wavelength λ_L, and thus contains many such coherent radiation segments. These coherent segments are separated longitudinally by the laser wavelength, and thus there exist $h\lambda_r$ radiation wavelengths of space between them. Therefore, if the

number of radiated cycles per coherent segment $N_{cyc} < h$, the output radiation profile will consist of a long train of coherent, fully separated pulses. This is the essential radiation profile of the scheme we propose.

We note that such a pulse train may also be obtained by a simple CHG beam traversing a short undulator. The method of this paper, however, allows pulse length control via the modulation amplitude with a single undulator, while altering the pulse length in the CHG method would require a new undulator for each desired pulse length.

Here we briefly illustrate the spectral mechanics of such pulse trains. We consider a pulse train made up of cosine waves of frequency ω_0, each contained within a Gaussian temporal envelope of width τ and separated temporally by h radiation cycles,

$$f(t) = \tau^{-1} \sum_{j=-N}^{N} e^{-(t-2\pi jh/\omega_0)^2/2\tau^2} \cos\left(\omega_0(t - 2\pi jh/\omega_0)\right)$$

Where $h, j \in \mathbb{Z}$, and $2N$ is the total number of pulses contained within the train. While these Gaussian modulated pulses are not entirely accurate for the pulse trains we will discover, this simple form yields the appropriate relationships between the various scales h,N, and ω_0.

We're interested in the spectral content of such a train, so the Fourier transform $\tilde{f}(\omega)$ is found as,

$$\begin{aligned}\tilde{f}(\omega) = &\left[\frac{1}{2}\left(e^{-\frac{\tau^2}{2}(\omega-\omega_0)^2} + e^{-\frac{\tau^2}{2}(\omega+\omega_0)^2}\right)\right] \\ &\times \left[\csc\left(\frac{\pi h\omega}{\omega_0}\right)\sin\left(\frac{\pi h\omega}{\omega_0}(2N+1)\right)\right]\end{aligned}$$

The first bracketed term comes simply from the truncated sine (the more familiar square wave window would produce a sinc function instead). The first term gives a Gaussian envelope with width $1/\tau$ centered on ω_0, while the second term involving $\omega + \omega_0$ can be neglected for envelopes covering more than one cycle. The second bracketed term is due to the pulse train character, and features multiple levels of harmonic spikes. This term can be though of as the result of a finite (only $2N$ spikes) version of the Dirac comb. There exist large scale spikes with the normal harmonic spacing at $\omega_n = \omega_0 + n\omega_0/h$, for integer n, appearing as the zeroes of the cosecant function. The width of these spikes is found by expanding around them $\omega = \omega_n + \delta\omega$ and finding the zero of the sine function. The result

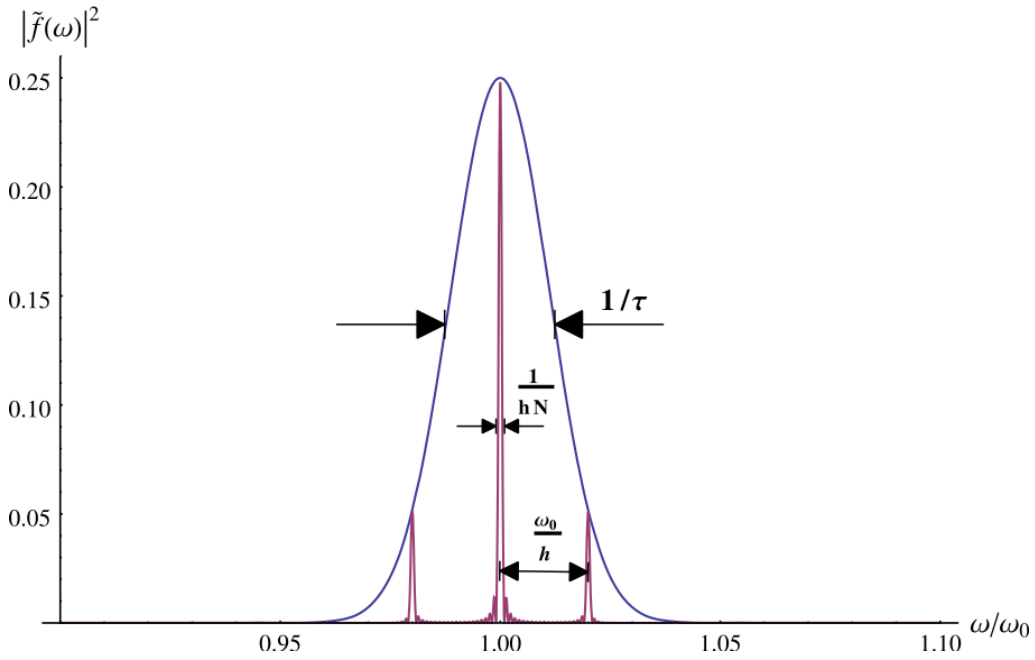

FIG. 3. Power spectrum of a short pulse train demonstrating the relationship between the different scales. The parameters here are $N = 10$, $h = 50$, and $\tau = 10\pi/\omega_0$. Given the artificially small N to illustrate the subharmonic width, some small sidebands are visible.

is a primary width of $2\delta\omega = 2\omega_0/(2N+1)h \approx \omega_0/Nh$, since N is generally large compared to unity.

Physically speaking, the sideband frequency of the harmonic spikes is determined by the temporal separation of the pulses, their spectral bandwidths are determined by the total number of pulses in the train, and all the harmonic spikes reside in an envelope determined by the temporal duration of each individual pulse. The relationship between these various frequency scales is shown schematically through the power spectrum $|\tilde{f}(\omega)|^2$ in Fig. 3.

The situation shown in Fig. 3 is representative of a train of pulses which never overlap temporally. As the duration of each pulse, here τ, approaches their temporal separation, $2\pi h/\omega_0$, the subharmonic peaks fall outside the Gaussian $1/\tau$ spectral bandwidth and the pulse train transitions to being essentially a single Gaussian-sine pulse with temporal duration $\tau \to N\tau$. This limit provides an essentially distinct, and generally unwanted, mode of operation when compared to the pulse train, and we will revisit it shortly in the context of our short-pulse generation scheme.

II. AN ANALYTIC MODEL

Our analytical model begins with the radiation field and motion due to a single electron in a planar undulator and closely follows the treatment in [17]. The resultant electric field due to the motion is described by the Liénard-Wiechert field,

$$\vec{E}(\vec{x},t') = \frac{1}{4\pi\epsilon_0}\frac{q}{c}\left[\frac{\hat{n}\times\left(\left(\hat{n}-\vec{\beta}\right)\times\dot{\vec{\beta}}\right)}{R'\left(1-\vec{\beta}\cdot\hat{n}\right)^3}\right]_{\text{ret}} \tag{1}$$

Where R' is the (retarded) distance from the source particle to observer, $\hat{n}$ is the unit vector in this direction, $\vec{\beta}$ is the normalized Lorentz velocity, q is the electron charge, and the subscript 'ret' indicates that the expression is to be evaluated at the retarded time t'. We have already omitted near field terms which scale like R^{-2}, as our analysis is strictly interested in the radiation in the far field. As a corollary, the motion of the electron in the magnetic field of the undulator is insignificant compared to the distance to the observer, and hence the vector $\hat{n}$ can be considered a constant, here taken to be in the $\hat{z}$ direction of a right-handed coordinate system. Correspondingly, the retarded distance R' is identified with some fiducial distance R, taken to be the distance between the observer and, for example, the center of the radiating undulator. The case of off-axis emission is treated in the appendix, and the results summarized in equations (A4)-(A6).

The motion in the undulator with undulator parameter K, period λ_u, and angular frequency $\omega_u \approx k_u c = 2\pi c/\lambda_u$ is described by the simple harmonic equations,

$$x(t') = \frac{K}{\gamma k_u}\cos(\omega_u t') \tag{2}$$

$$z(t') = \bar{v}_z t' + \frac{K^2}{8\gamma^2 k_u}\sin(2\omega_u t') \tag{3}$$

With the averaged z velocity $\bar{v}_z$ given by

$$\bar{v}_z = c\left(1-\frac{1}{2\gamma^2}\left(1+\frac{K^2}{2}\right)\right) \tag{4}$$

We are now assuming that the electron traversing the undulator is fairly relativistic and keep terms up to order γ^{-2}. Performing the vector arithmetic with these trajectories in equation (1) and taking only the leading terms in γ, we get an electric field purely in the $\hat{x}$ direction given by,

$$E_x(t') = \frac{4q\gamma^3 K k_u}{\pi\epsilon_0 R}\cos(\omega_u t')\left[\frac{2-K^2+K^2\cos(2\omega_u t')}{\left(2+K^2-K^2\cos(2\omega_u t')\right)^3}\right] \tag{5}$$

The bracketed term corresponds to the searchlight wiggler effect for high K values and serves to slightly modify the sinusoidal shape. We are primarily concerned with the frequency shift of the sine wave, which is not affected by this extra term, hence for simplicity it is averaged over one period to a value of $\overline{[\cdots]} = \frac{1}{16}\left(1+K^2\right)^{-5/2}\left(4+2K^2+K^4\right)$. In the ultrarelativistic approximation on axis we have the retarded time t' related to the time of observation t as,

$$t = \left(1+\frac{K^2}{2}\right)\frac{1}{2\gamma^2}t' \tag{6}$$

Next, we introduce an energy offset from some nominal Lorentz factor $\gamma = \gamma_0 + \delta\gamma$ and expand, keeping only terms linear in $\delta\gamma$,

$$E_x(t) = \frac{q\gamma_0^3\left(1+3\delta\gamma/\gamma_0\right)\tilde{K}k_u}{\pi\epsilon_0 R}\cos(\omega_r t(1+2\delta\gamma/\gamma_0)) \tag{7}$$

With the definition,

$$\tilde{K} = K\left(1+\frac{K^2}{2}+\frac{K^4}{4}\right)\left(1+K^2\right)^{-5/2} \tag{8}$$

And the resonant frequency ω_r defined as,

$$\omega_r = \frac{2\gamma_0^2\omega_u}{1+K^2/2} \tag{9}$$

This is the electric field from a single electron traversing the undulator. We now generalize this description to a continuous distribution of electrons which are distributed in longitudinal position as in a finite length electron beam. The longitudinal position is quantified by an initial phase offset ϕ_0 relative to the resonant frequency, $\omega_r t \to \omega_r t - \phi_0$. This phase can be thought of as a time offset for when the different electrons enter and exit the undulator. In addition to this phase, the electron distribution may also contain energy deviations $\delta\gamma$ from the nominal value of γ_0 which may be correlated with the phase ϕ_0.

With such a distribution in mind, we consider that the effect we are interested in involves the slippage between the different electrons in the beam. It is clear to see, from the $\delta\gamma/\gamma_0$ term in the cosine of equation (7), that particles with different energy deviations evolve in the phase of the cosine wave at different rates. We can expect coherent emission from the electron distribution when all these phases are similar for a short duration of time. Therefore, it is the energy variation inside the cosine which will produce the coherent radiation effect. By contrast, the amplitude variation in equation (7) leads to small variations in the amplitude of radiation for different electrons. However, unlike the phase inside the cosine, there is no possibility for these variations to combine coherently, and they serve only to alter slightly

the amplitude of the coherent effect. Therefore, in what follows we ignore (or average over) this amplitude variation, instead approximating it as a constant.

For a laser modulated electron distribution the quantities $\delta\gamma$ and ϕ_0 are not independent, and we choose to express $\delta\gamma(\phi_0)$. The electric field from an individual electron can then be written in terms of ϕ_0 as,

$$E_x(t,\phi_0) = E_0 \cos\left(\omega_r t\left(1 + 2\delta\gamma(\phi_0)/\gamma_0\right)\right) \tag{10}$$

The coefficient $E_0 \equiv \frac{q\gamma_0^3 \tilde{K} k_u}{\pi\epsilon_0 R}\left(1 + 3\delta\gamma/\gamma_0\right)$ has collected everything besides the ϕ_0 dependent term for convenience. The total electric field from the entire electron distribution can then be written as an integral over the distribution in ϕ_0 of the individual electric fields $E_x(t,\phi_0)$,

$$E_{\mathrm{TOT}}(t) = \int E_x(t,\phi_0)\rho(\phi_0)d\phi_0 \tag{11}$$

Where $\rho(\phi_0)$ is the normalized density distribution of particles with respect to the phase ϕ_0. All that is left to specify is $\delta\gamma(\phi_0)$, which describes how the electron distribution is prepared, and $\rho(\phi_0)$, which is assumed to be a flat distribution as a function of ϕ_0 since the electrons are not initially bunched on the radiation wavelength scale.

A. Linear Model

A linearly chirped beam was previously considered in [18]. This study analyzed the coherent emission of a single, linearly chirped Gaussian current electron beam inside a radiating undulator. This single-segment situation could conceivably be produced by a strong RF chirp over the entire electron beam, as the pulse train aspect of the beam was not considered. A linear model also serves as an approximation to the electron dynamics near the $s \approx \lambda_L/2$ portion of the sinusoidal modulation shown in Fig. 2. We consider a linear variation in of energy with the phase modeled as,

$$\frac{\delta\gamma}{\gamma_0} = A\frac{\phi_0}{h} \tag{12}$$

The factor of h has been included as a reference to the quasilinear chirp of a sine wave of frequency $1/h$ times the undulator radiation frequency. As previously mentioned, with such a scenario particles are evenly distributed in phase so that $\rho(\phi_0) = N_p/(2h)$, with N_p

the number of particles, so we have,

$$E_{\mathrm{TOT}}^{\mathrm{lin}}(t) = \frac{E_0 N_p}{2h} \int_{-h}^{h} \cos\left(\omega_r t \left(1 - \frac{2A}{h}\phi_0\right) - \phi_0\right) d\phi_0 \tag{13}$$

where the limits are chosen in the range $(-h, h)$ such that the energy modulation ranges from $(-A, A)$ to approximate the linear portion of a sine-wave modulation of amplitude A. The integrated field from a single chirped electron bunch is then,

$$E_{\mathrm{TOT}}^{\mathrm{lin}}(t) = N_p E_0 \cos(\omega_r t)\mathrm{sinc}(h - 2At\omega_r) \tag{14}$$

From the sinc function modulation we deduce the duration of the pulse $t_p \approx \pi/A\omega_0$, or alternatively, that the number of emitted cycles is,

$$N_{\mathrm{cyc}} \approx \frac{1}{2A}$$

From this we also learn the frequency bandwidth of the power spectrum ($P(\omega) = |\int E(t)e^{i\omega t}dt|^2$) signal to be

$$\frac{\Delta\omega}{\omega_r} \approx 4A$$

We thus arrive at the same essential scaling that we developed in our introduction: The number of coherent radiation cycles is inversely proportional to the modulation amplitude. In fact, to this level of detail the results are identical.

B. Sinusoidal Laser Modulation

The far more relevant physical case is that in which a laser interacts with the electron beam inside a short undulator to imprint on it a sinusoidal energy modulation. For this case, in contrast to equation (12), we have the more general expression,

$$\frac{\delta\gamma}{\gamma_0} = A \sin\left(\frac{\phi_0}{h}\right) \tag{15}$$

Again, the factor of h here clearly appears as the scale between the undulator radiation phase and the laser phase, and is identical to the harmonic of the laser being used compared to the undulator radiation wavelength: $\lambda_L = h\lambda_r$. The total field is then given by,

$$E_{\mathrm{TOT}}^{\mathrm{sin}}(t) = \frac{N_p E_0}{2h} \int_{-h}^{h} \cos\left(\omega_r t \left(1 + 2A \sin\left(\frac{\phi_0}{h}\right)\right)\right) d\phi_0 \tag{16}$$

As with the linear case, the normalized density distribution is independent of the initial phase, so $\rho(\phi_0) = N_p/2h$. The nested sine functions can be dealt with by expanding in terms of Bessel functions J_n, in particular with the relation,

$$e^{i2A\omega_r t\sin(\phi_0/h)} = \sum_{n=-\infty}^{\infty} J_n\left(2A\omega_r t\right) e^{in\phi_0/h}$$

The integration over the phase ϕ_0 is here carried out over a single laser wavelength, and if we assume the harmonic upconversion h to be relatively large, we may use $(-\infty, \infty)$ as the limits of integration to simplify the result. In this case, all but one of the Bessel modes drops out of the calculation and we are left with,

$$E_{\mathrm{TOT}}^{\sin}(t) = N_p E_0 \cos\left(\omega_r t\right) J_h\left(2A\omega_r t\right) \tag{17}$$

The form of the net electric field is conceptually identical to the linear case in equation (14), except instead of a sinc function we have J_h providing the modulation envelope. To connect with both experiment and simulation, however, we note that our result in equation (17) is valid only for a single laser wavelength of the electron bunch. We then sum up each contribution with an appropriate shift in the time domain to obtain the total signal,

$$E_{\mathrm{bunch}}(t) = \sum_j E_{\mathrm{TOT}}^{\sin}(t - 2j\pi h/\omega_r) H(t - 2j\pi h/\omega_r) \tag{18}$$

Where $H(t)$ is the Heaviside step function, and the sum over j extends far enough to cover the entire electron beam. Already from these solutions we can see that there will be a delay in the emission, since the Bessel function has its maximum when its argument is approximately equal to its order, one must wait until $t \approx \frac{h}{2A\omega_r}$, which is the same condition derived from the linear case. This delay is physically represented by having to wait for the electron distribution to shear over from panel (a) in Fig. 2 to panel (b). This delay can be removed, if it is large, by using a pre-bunching chicane as shown in Fig. 1 to enter the radiating undulator with a distribution close to panel (b) of Fig. 2, thus entering the coherent radiation regime almost immediately.

The production of a pulse train of few-cycle pulses, as opposed to a long radiation pulse defined by the electron bunch length, is governed by the relationship between A and h. The condition can be thought of, roughly, as $N_{\mathrm{cyc}} < h$ for the pulses to be non-overlapping. Using the schematic dependence in the introduction, this condition can be rewritten as,

$$\frac{1}{2} \lesssim Ah \tag{19}$$

When this condition is satisfied, the radiation pulses from each laser wavelength (each compressed region in Fig. 2) will be separated from one another. This condition can be satisfied by freely tuning both the modulation amplitude and harmonic upconversion, although in practice the transport of beams with $A \gtrsim 0.1$ may prove challenging.

Although an analytical Fourier transform is not readily available, we can still make several statements about the form of the power spectrum. The pulse-train inherent in equation (18) leads to harmonic peaks at regular intervals of ω_r/h (the laser frequency harmonics) which will in general be quite sharp with width inversely proportional to the electron beam length. These harmonic peaks are feature of the pulse train created by the long electron bunch with independent radiating sections, and will be superimposed on top of a background spectrum (for comparison, this background spectrum is the Gaussian envelope in the example of the introduction pulse train and Fig. 3). In our present case, this background spectrum is characterized by the Bessel function, which leads to a characteristic two-horned shape as opposed to a sinc function more common from a finite undulator. We estimate the width of this Bessel pedestal by approximating the first Bessel function zeroes j_h, and the zeroes of its first derivative j'_h [19],

$$j_h \approx h + 1.85h^{1/3}$$

$$j'_h \approx h + 0.808h^{1/3}$$

Thus we approximate the full width of the Bessel function peak during which substantial coherent radiation takes place, and, assuming a transform limit, obtain a full-width of the power spectrum,

$$\frac{\Delta\omega}{\omega_r} \approx 2\pi A h^{-1/3} \tag{20}$$

Unlike the estimate from the linear modulation, here we pick up a slight dependence on the harmonic upconversion factor which tends to narrow the spectrum for high harmonics. This dependence is due to the nonlinearity of the sheared over sine wave in longitudinal phase space, which is encoded in the Bessel function. As the harmonic factor increases, the nonlinearities are increasingly on a scale larger than the coherence length. On the other hand, for small harmonic factors the nonlinear curvature quickly spreads the electrons outside the coherence length, leading to a shorter pulse of coherent radiation.

We can calculate the energy density contained in the signal using the electric field (17)

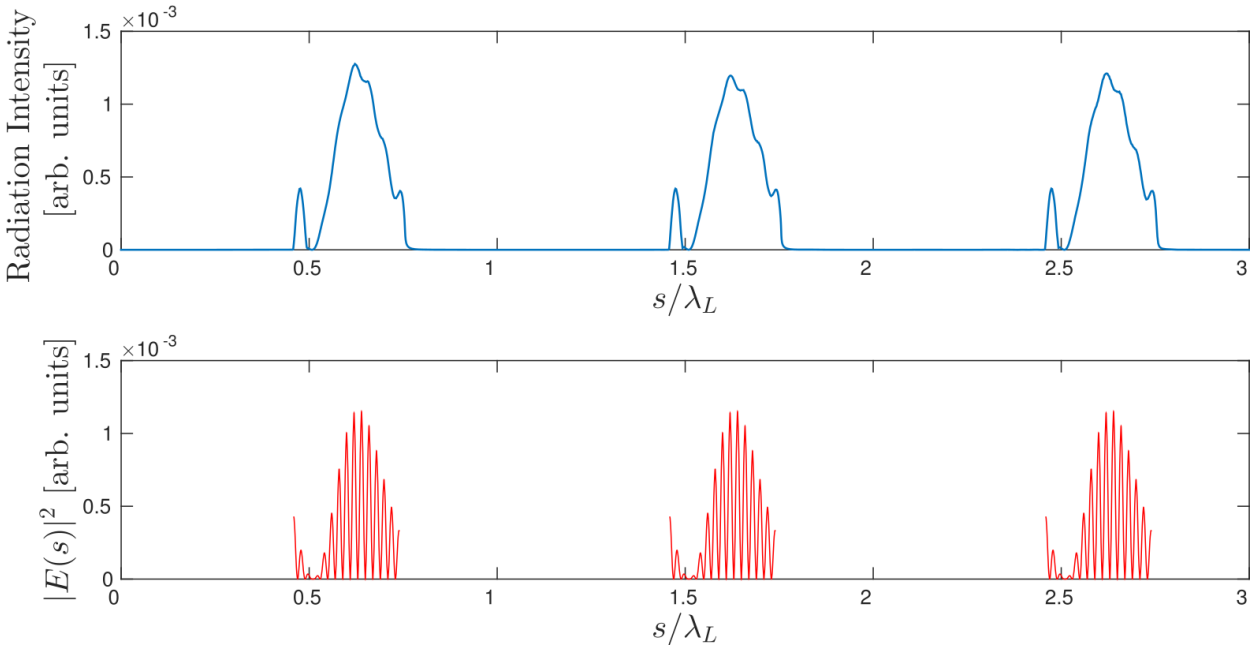

FIG. 4. Comparison of the electromagnetic field intensity from Puffin (top) and the analytical formula (18) (bottom) for the squared electric field showing the pulse train structure. The longitudinal extent of this plot covers three laser wavelengths, and the harmonic upconversion factor is 25. Note that from the definition of s, the radiation slips to the right in this plot, so the most recent radiation is found at the left-most portion of the pulses.

from,

$$\mathcal{E} = \int_0^{t_{\text{final}}} \frac{1}{2Z_0} |E(t)|^2 dt \tag{21}$$

Where $Z_0 \approx 377\Omega$ is the impedance of free space, and the time integral should extend over the duration of emission. For a typical case, we consider a modulated beam which is allowed to disperse in the radiating undulator through only the first Bessel peak, giving a final time $t_{\text{final}} \approx \frac{1}{2A\omega_r}(2\pi + h)$. With the reasonable assumption that the duration of coherent emission persists for several radiation periods, and integrating over a spherical shell of radius R through angles $\theta < \gamma_0^{-1}$ the total pulse train energy is given by ,

$$\mathcal{E} = \frac{N_p^2 \langle E_0^2 \rangle}{16\sqrt{\pi}\gamma_0^2 Z_0 A\omega_r} X(h) \tag{22}$$

Where $X(h)$ is a universal, slowly varying function of h shown in Fig. 10 and the functional form given in equation B4 of the appendix. The number of particles N_p should be taken to be the number in one modulation wavelength, and for a long beam should be summed up with appropriate weights corresponding to the current profile. The inverse dependence

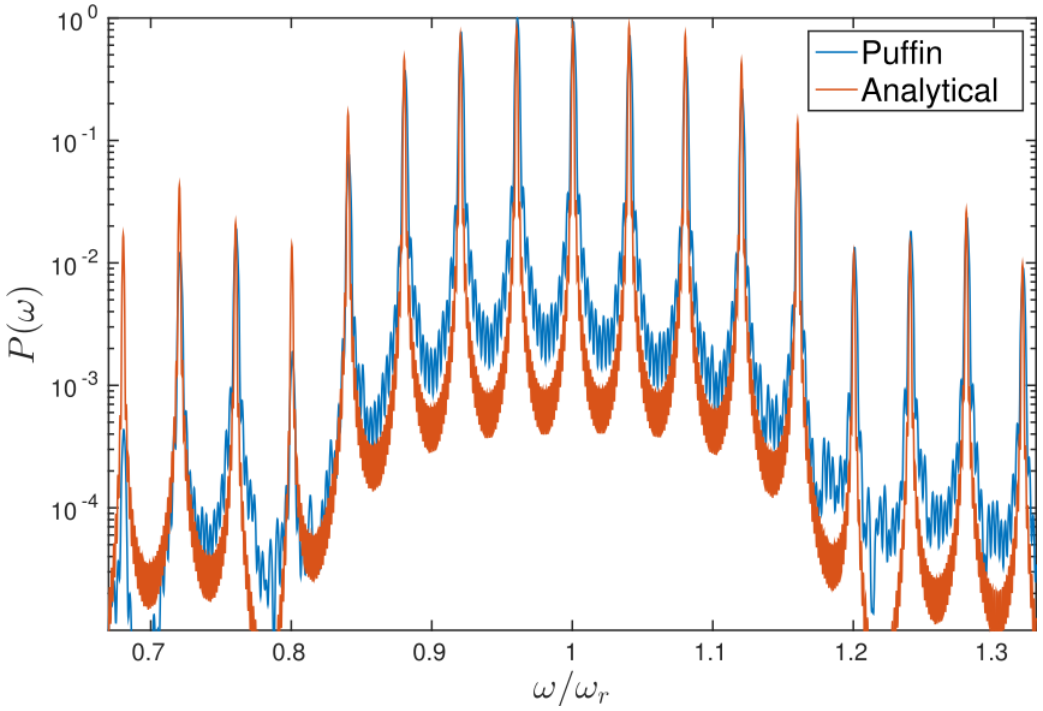

FIG. 5. Comparison of the computational power spectrum obtained from Puffin and the analytical estimate based on equation (18). The power spectra are normalized to their maxima. The electron beam has $A = 0.09$ and is run through 7 undulator periods.

on the modulation amplitude A is understood as larger values of A lead to shorter pulses, and assuming approximately equal power, a smaller total energy. We briefly note that the averaged quantity $\langle E_0^2 \rangle \propto (1 + 9A^2/2)$ contains a weak dependence on the modulation amplitude A, since A is quite small compared to unity.

III. COMPARISON WITH SIMULATIONS

The electric field, given by equation (18) is compared with a numerical simulation using the 3D unaveraged FEL code Puffin [20]. Since the effect we are interested in involves only longitudinal dynamics, for computational efficiency we use only the 1D mode of the Puffin code, in which the transverse dimensions are neglected. Furthermore, to facilitate comparison with the analytical model developed, we disable the FEL interaction and operate the simulation at low peak current to study only the coherent radiation effects. We consider an electron beam with $\gamma = 401.608$ in an undulator with $K = 1.26$ and period $\lambda_u = 1.8$cm, essentially the parameters of the VISA undulator resonant at 100 nm [21]. The electron

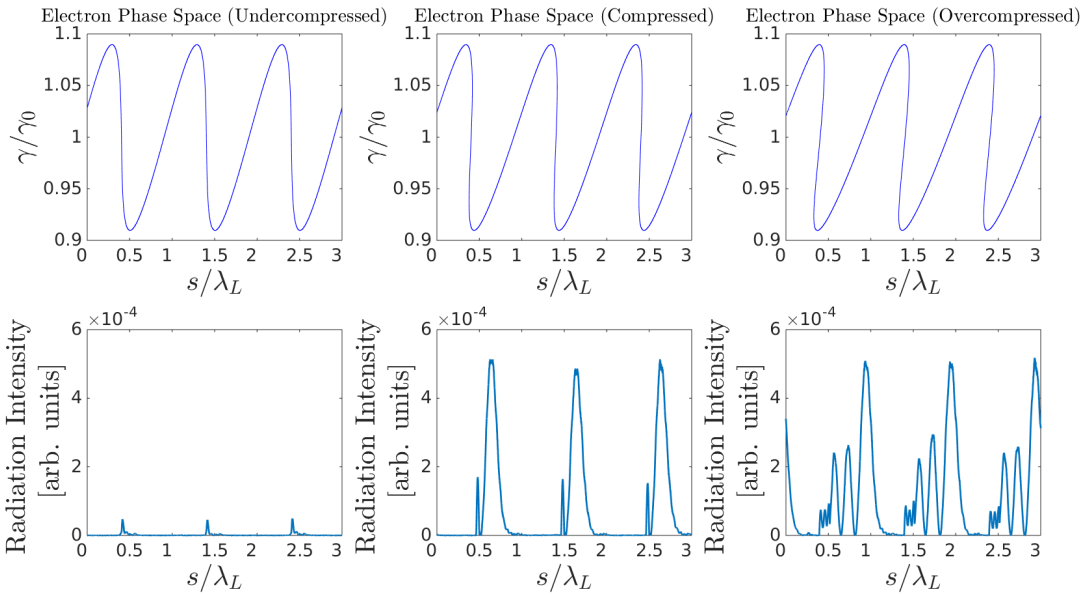

FIG. 6. The electron beam longitudinal phase space (top row) and field intensity profile (bottom row) as the beam traverses the undulator. The beam is first undercompressed and does not radiate significantly (left, 2 undulator periods), before it becomes optimally compressed and radiates strongly (middle, 12 undulator periods). If allowed to continue, the beam will radiate the lower intensity, subsequent Bessel peaks (right, 20 undulator periods).

beam has an approximate length $c\tau = 20\mu$m, possesses negligible current and emittance, and has a relative energy spread of 10^{-5}. The electron beam is modulated with a 2500 nm laser, giving a harmonic upconversion factor $h = 25$, and attains a maximum modulation $A = 0.09$. Finally, a magnetic chicane is used to 'pre-bunch' the beam to close to the coherent radiation point to limit simulation time. A comparison of the electric field from the analytical expression of equation (18) with the radiation intensity is shown in Fig. 4, while a comparison of the analytical and computational power spectra is shown in Fig. 5.

For the full field comparison, the squared electromagnetic field amplitude is plotted against the longitudinal coordinate s scaled to the laser wavelength λ_L. From the analytical expression, the individual cycles are resolvable, whereas the Puffin simulation yields a smoothed intensity over individual radiation cycles. We clearly observe the first Bessel peak in both the analytical and numerical field amplitudes, and the pulse train structure is clearly visible. Note that the simulation was terminated after 7 undulator periods, corresponding to the approximate width of the first Bessel maximum, although we observe the

second Bessel peak beginning to develop.

The relationship between the electron beam phase space and the generation of the radiation pulses is shown clearly in Fig. 6. We see that the maximum compression, as shown schematically in Fig. 2, corresponds to the generation of the main pulse of radiation. If the undulator is not terminated after this point, as it was in Fig. 4, the electron beam will continue to radiate at lower intensity on subsequent Bessel peaks, as shown in the right-most panel of Fig. 6. It is therefore not necessary to terminate the undulator after precisely the first Bessel peak, as the subsequent radiation preserves the pulse train structure if it is for a sufficiently short duration.

There is excellent agreement between the computational and analytical power spectra in Fig. 5, and there are several features of note. First, the various harmonic spikes appear naturally as the various harmonics of the seed laser as one would expect from an HGHG type source. However, from equation (18) we see the same harmonics arise as the simple result of a train of radiation pulses, all at the same frequency ω_r and temporally separated by $2\pi h/\omega_r$, the fourier transform of which produces submodal spacing at intervals $\Delta\omega = \omega_r/h$. We note that because of the short length of the electron bunch (roughly a dozen laser wavelengths), the subharmonic peaks possess significantly larger width (consistent with Fig. 3) than they otherwise would with a more typical ps long electron beam (compare with Fig. 9).

We also note the expected width of the main spectral envelope, which is here composed in equal part of the short undulator length as well as the temporal width of the first Bessel function peak. To verify the relationship between this spectral width and the harmonic factor, we run a series of simulations with $A = 0.09$ and various harmonic factors, each of which passes through a 14 period undulator after having been sufficiently pre-bunched. The results in figure 7 confirm that equation (20) is quite a good estimate of the full-width bandwidth of the power spectrum and the $h^{-1/3}$ dependence is particularly evident.

IV. DELETERIOUS EFFECTS

The analytical model of section II and computations of section III have neglected several physical effects which potentially conspire to harm the coherent pulse train effect.

First, the modulation of the electron beam by several percent of its total energy presents its own challenges. Broadly speaking, when interacting a laser with an electron beam in an

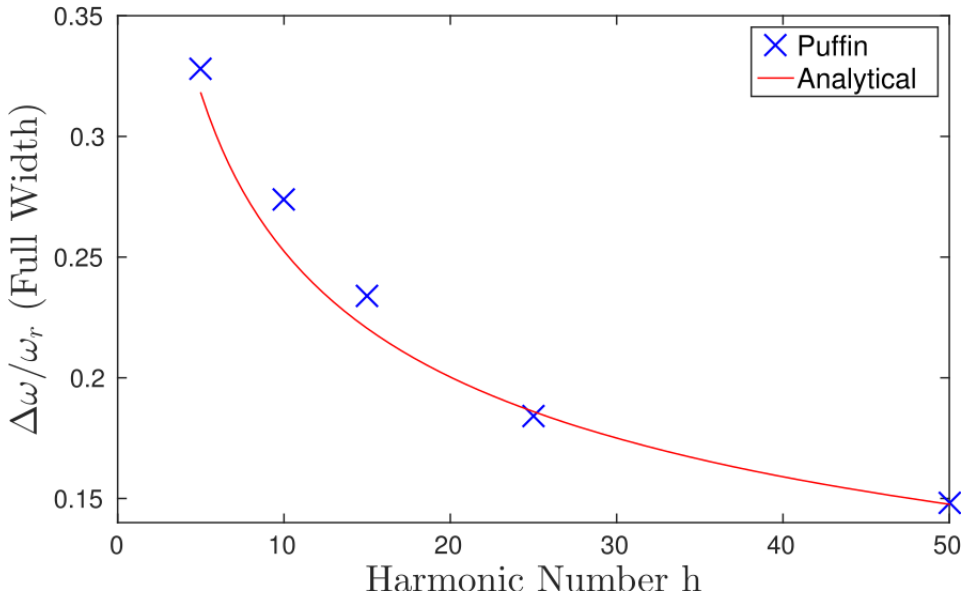

FIG. 7. Comparison between computational power spectrum full width (blue markers) and the analytical estimate based on equation (20).

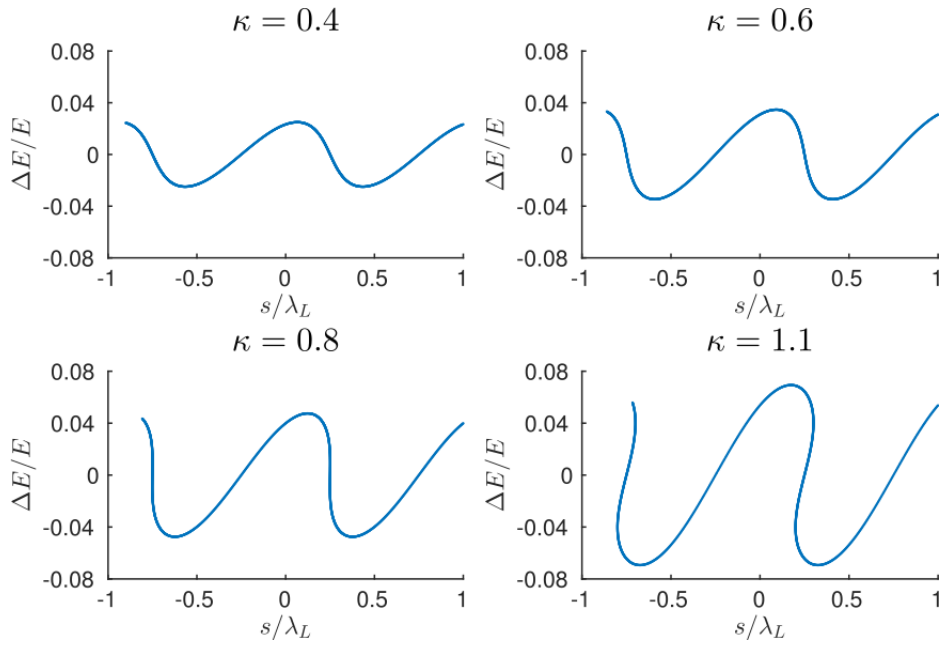

FIG. 8. The development of a non-sinusoidal energy modulation inside of the modulating undulator. The energy modulation normalized to the total beam energy is shown against the longitudinal coordinate scaled to the laser wavelength. We begin to see the folding over of phase space for $\kappa \gtrsim 1$.

undulator, the maximum sine-like modulation amplitude A achievable scales inversely with the number of periods $A \sim 1/4N_u$, i.e. the modulation must be achieved in fewer than $1/4A$ undulator periods due to slippage within the modulating undulator. If more periods are used, the phase space will fold over and become highly non-sinusoidal.

We can quantify this non-sinusoidal scale by introducing the parameter $\kappa \equiv 4AN_u$, so that we require $\kappa < 1$ for a reasonably sinusoidal modulation. The dependence of the modulation profile on κ is shown for some simulations in Fig. 8, in which it is clearly seen that for $\kappa > 1$, the phase space becomes quite non-sinusoidal. Note that the produced longitudinal phase space is not equivalent to a sheared sine-wave, as in Fig. 2. Rather, because the electrons slip considerably with respect to the laser phase, the beam acquires a somewhat more bulbous character, which can be seen developing in the final plot of Fig. 8. Of course, if the factor κ becomes much larger than unity, the electrons will begin to fill out the buckets in laser phase as is common in inverse FEL accelerators [22] and conventional RF accelerators [23]. Note that this discussion assumes the laser field amplitude to be uniform over the duration of modulation. In the case that the laser field diffracts away prematurely, the full modulation amplitude A is reached before the end of the undulator. In effect, this allows additional undulator length through which the electrons will disperse, possibly prematurely shearing over the electron beam as shown in the last panel of Fig. 2. This undesirable effect could be limited by achieving the required modulation in the shortest undulator possible, or by focusing a diffracting laser beam towards the exit of the undulator.

A related issue is that depending on the laser wavelength and modulation amplitude, the required drift from modulator to radiator may provide a tight requirement on the floor space requirements of this setup. In the ultra-relativistic regime the transport matrix R_{56} for a drift of length L is given by $R_{56} = L/\gamma_0^2$. To illustrate the point, using a 100 MeV beam and an 800nm laser with a modulation amplitude $A = 0.05$, less than 15cm is allowable between the modulating and radiating undulators. This requirement arises as the electron beam must not shear over through the coherent regime before reaching the radiating undulator. Of course, these requirements are mitigated when using a higher energy electron beam or longer wavelength laser, but remain an important consideration for constructing an experimental setup utilizing this effect. Depending on the particular setup, then, it may not even be necessary to include a 'pre-bunching' chicane, as is shown in Fig. 1. Due to this practical concern, as well as the fact that all effects considered in this paper happen on a relatively

short timescale, we do not consider any possible collective effects arising due to the use of a chicane.

The modulation of the electron beam on the order of several percent of its total energy, and subsequent compression, potentially also leads to very high currents and space charge instabilities. In the absence of space charge, an electron beam with modulation amplitude scaled by the slice energy spread, $B \equiv \Delta E/\sigma_E$, when fully compressed by a linear dispersion, produces a peak current enhancement [24],

$$\frac{I_{\text{peak}}}{I_0} \approx \frac{eB}{1+B^{1/e}} \tag{23}$$

Where I_{peak} is the peak current, and I_0 is the nominal uncompressed current. To take a typical example, an electron beam generated from a photocathode may have, after boosting to ∼100MeV, a slice energy spread $\sigma_E/E \sim 10^{-5}$. This beam could be modulated by several MeV, leading to a value of $B \sim 10^3$. From equation (23), we would expect compression by a factor of hundreds, which for an initially reasonable beam current can reach the problematic range of tens of kA.

The effect of transverse space charge can be approximated as an associated transverse emittance growth in a drift of length z, which can be found as [25],

$$\Delta\epsilon_n(z) = \frac{Ig}{4I_A\beta^2\gamma^2}z \tag{24}$$

where $I_A \approx 17$kA is the Alfvén current, I is the beam current, β is the normalized electron velocity, and g is a geometric factor of order unity. The drift length z over which the emittance increase will occur can be found as the length through which the particles drift before decompression occurs. The width of the current peak (in the lab frame) obtained by a beam modulated at laser wavelength λ_L is approximately $\Delta z = \lambda_L/2B$, and the longitudinal drift rate is given by $A(dR_{56}/dz) = A/\gamma^2$, yielding a drift length. The result is an emittance increase,

$$\Delta\epsilon_n = \frac{g\lambda_L}{8\beta^2 AB}\frac{I}{I_A}$$

Note the result is (nearly) independent of beam energy, as we have assumed the beam to be relativistic. Inserting some typical values, $A = 0.05$, $B = 10^3$, $\lambda_L = 10.6\mu$m, the emittance increase is found to be 0.7nm/kA. Given the typical normalized emittance of linear machines on the order of one micron, we conclude that the transverse space charge effect is negligible for the cases we are interested in.

The longitudinal space charge (LSC), however, has the effect of limiting the peak current, and potentially destroying the longitudinal phase space necessary for coherent emission. We measure the effect of the LSC by the limit it imposes on the peak current attainable. The energy change produced by the LSC can be estimated for a parabolic current profile of peak current I_{peak} and length δ as [26],

$$\Delta E = \frac{3}{4\delta}\frac{eI_{\text{peak}}}{8\pi\epsilon_0\beta^2\gamma^2 c}z \tag{25}$$

where we have dropped a term which is logarithmic in the ratio of the beam pipe diameter to the transverse beam size. We note that there is a 3D correction the simple formula of equation (25) controlled by the parameter $\xi = kr_b/\gamma$, where k is the wavenumber of interest and r_b the transverse beam size [27]. These corrections are important for the fine-scale structure of the bunching introduced by the LSC, and become relevant for $\xi \gtrsim 1$. We neglect such corrections here, choosing to ignore the fine-scale structure that may arise in order to arrive at a simple scaling law regarding the maximum compressibility of the beam.

Proceeding in analogy to the transverse space charge, the drift distance z is taken to be the beamline distance over which the particles drift through the distance $\delta/2$. This forms a first approximation for the effect, as in reality as ΔE decreases, the particles will drift slower and the beam distribution becomes highly non-symmetric. Nevertheless, setting the energy loss equal to the modulation energy, $\Delta E = A\gamma mc^2$, we arrive at an LSC dominated peak current,

$$I_{\text{peak}} = \frac{16}{3}I_A\beta^2\gamma A^2 \tag{26}$$

This current is not exactly a peak value in reality, but more accurately represents the value near which LSC oscillations cannot be ignored. Above this value, the LSC dominates the longitudinal dynamics of the beam, making invalid the coherent analysis of section II. By virtue of this, this current is the peak (compressed) current which can be used to create the short pulse coherent emission. A full simulation including the effect of LSC would elucidate the effect on the coherent emission in the cross-over regime, but the code Puffin does not currently support LSC modeling. Therefore, we consider our results generally valid only below this LSC dominated peak current.

Beyond these space charge effects, we also note that the non-linear transport component present in a real machine has the potential to become important for energy deviations of several percent. The non-linear effects manifest here as the 2nd order transport element

T_{566}, defined as $\frac{1}{2}\frac{\partial^2 s}{\partial(\delta p/p)^2}$. A numerical analysis of the compression in a drift including the T_{566} transport component was performed to study this possibility. We observed only a few percent degradation compared to equation (23) and the simulations including only R_{56}, even with modulation amplitudes up to 10%. The fact that peak current is not significantly degraded due to the T_{566} component of transport also suggests a minimal impact on the coherent emission studied in this paper.

A more serious, although purely practical, effect is due to the finite laser spot size in the modulating undulator. Since we are dealing with modulations much larger than the intrinsic slice energy spread of the beam, we must also consider the non-uniformity of the modulation itself. In effect, the non-uniformity of the laser modulation can be understood as an effective increase in the beam slice energy spread, and hence a decrease in the parameter B which determines the peak current by equation (23).

To understand this effect, consider a transversely Gaussian electron beam with standard deviation σ_b which is modulated by a Gaussian laser beam with transverse standard deviation σ_L. Combining these two distributions, we find the point at which the resultant function drops to $1/e$ its peak value to define its standard deviation. The result is an effective energy spread increase σ_E^{laser} from a laser with modulation amplitude ΔE and wavevector k_L, depending on the ratio between the two length scales $f \equiv \sigma_L/\sigma_b$,

$$\sigma_E^{\text{laser}}(s) \approx \Delta E \sin(k_L s)\left(1 - e^{1/(1-f^2)}\right) \tag{27}$$

The result is an energy spread which is dependent upon the transverse bunch position, which combines in quadrature with the intrinsic slice energy spread of the electron beam. A full analysis of the maximal compression of such a bunch is outside the scope of this paper, so we simply report numerical results.

To get a feel for this effect, consider $B = 10^3$, and $f = 5$, which seems reasonable for an electron beam of size 200μm modulated by a laser with spot size of 1mm. For reference, such a situation in which the electron beam has mean energy 100MeV, slice energy spread 1keV, and is modulated by 1MeV produces a maximal laser induced energy spread $\sigma_E^{\text{laser}} \approx 40$keV, 40 times the initial slice energy spread. Nevertheless, simulations show that peak compression is reduced from the case of $f \to \infty$, which provides $I_{\max}/I_0 \approx 190$, to $I_{\max}/I_0 \approx 95$ for $f = 5$, almost a factor of two. Even a relatively 'safe' choice of $f = 10$ produces only 80% the maximal peak current due to this effect, while a tightly focused laser

with $f = 2$ produces only 17% the peak current.

Even if the production of the individual radiation pulses is not inhibited, the fixed-phase relationship between all the pulses in the train may be disrupted by irregularities on the scale of the electron beam. Electron beam chirp or quadratic curvature in energy do not present a significant problem, as the imposed energy modulation is generally much larger than the chirp or curvature produced in normal operation modes via RF structures. Variation in the laser temporal intensity, however, is a much larger concern, as differing modulation amplitudes across the beam will cause coherent emission both at differing locations along the undulator and of differing duration.

We can estimate that this effect will become completely destructive when one portion of the beam (modulated at amplitude A) has already passed through its coherent radiation phase while a second part (modulated at $A - \delta A$) has not even begun its coherent radiation. From the simple analytical scaling in the introduction, we deduce the criterion,

$$\delta A \ll \frac{2\pi A}{h}$$

For parameters where A is several percent and h is around a dozen, this implies a control on δA on the order of one percent. For Gaussian shaped electron beams and laser pulses, this puts a practical constraint that the RMS length of the laser pulse should be on the order of tens of times longer than the electron bunch to ensure good phase coherence between the majority of the radiation pulses.

While some of these effects clearly have more destructive potential than others, all of them can be eliminated or mitigated in practical setups by appropriate choice of laser and electron beam parameters.

V. EXPERIMENTAL PROSPECTS

We consider an experimental setup analogous to that studied in section II. This setup could be realized at Brookhaven National Laboratory's Advanced Test Facility (ATF) using a 10.6μm CO_2 laser to modulate a 60MeV electron beam in a few period undulator such as the electromagnetic STELLA prebuncher [28]. With a laser power of a few hundreds of GW and a spot size of a few mm, modulation amplitudes up to $A = 0.1$ are possible, although we consider a more likely working point of $A = 0.04$. To provide a high harmonic

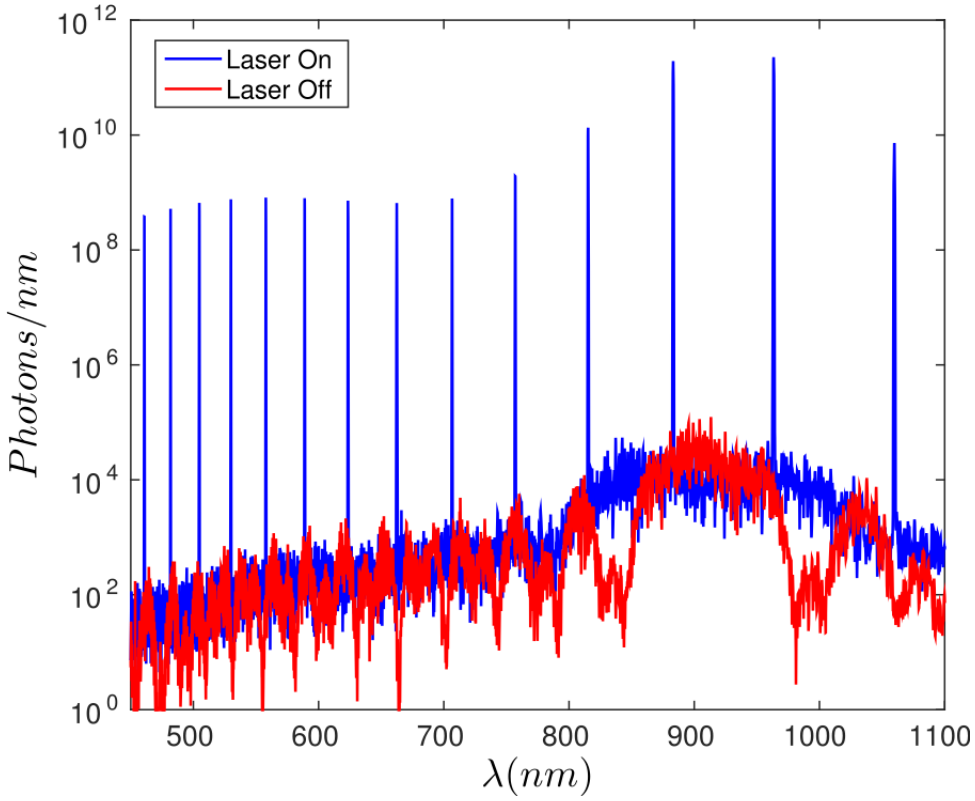

FIG. 9. The resultant power spectrum from the proposed experimental setup at the ATF. The y-axis is the number of photons per nm bandwidth. Spectral brightness is increased by 6 orders of magnitude for the laser harmonics, while integrated radiation energy is increased by roughly 4 orders of magnitude.

upconversion, a small-period undulator could be used to support radiation wavelengths as low as $\sim$ 900nm, near the 11^{th} and 12^{th} harmonics of the seed laser.

A simulation of this setup at the ATF was performed using Puffin with an idealized electron distribution. A modulation of $A = 0.04$ is imprinted on the beam by the CO_2 laser, which then radiates in a 12 period helical undulator with $K = 0.82$ and $\lambda_u = 1.9$cm. The electron beam has characteristic parameters of the ATF with normalized emittance of 2μm, charge of 100pC, relative energy spread of 10^{-4}, and rms bunch length of 3ps. The resultant power spectrum is shown in Fig. 9, with a comparison to the spontaneous signal produced with no laser interaction.

The harmonics spikes in the ATF setup spectrum are quite sharp compared to the sample simulation of Fig. 5 due to the realistic bunch length containing roughly a hundred separate radiation regions. For this case, the individual spikes are about 1 nm wide, which is in good

agreement with the expected $1/hN$ estimate from the introduction. For this experiment, the total pulse train energy from equation (22) is 66 nJ, while the Puffin simulations yield a total energy of 52 nJ – a reasonable agreement given the approximations in equation (22). For reference, the spontaneous radiation energy is only 11 pJ.

The resultant spectrum from an ATF-scale experiment is reminiscent of HHG sources, which are capable of producing a train of attosecond pulse trains with harmonic content down into the extreme ultraviolet wavelength range [29]. Furthermore, as in the case of the effect in this paper, the individual radiation pulses are in a phase-matched relationship [30], strengthening the analogy between the two methods of harmonic radiation production. The total energy of ≈50 nJ produced in the ATF experiment compares favorably to HHG sources which, depending on the configuration, may produce anywhere from nJ to μJ of total energy in the harmonics [31]. However, for the above configuration, conversion from laser energy into harmonics (the electron beam carries only a small fraction of the laser beam energy in this setup) is only 10^{-8}, while HHG sources typically produce conversion efficiencies on the order of $10^{-5} \sim 10^{-6}$. We note, however, that large gains in efficiency can be obtained by simply increasing the electron beam charge due to the coherent nature of the emission, as seen from equation 22.

VI. CONCLUSION

We have described a novel method for the generation of few-cycle pulse trains of coherent radiation. We developed a simple analytical model which yields generic predictions, found to be in good agreement with simulations. The method is ultimately based on strongly modulating an electron beam and allowing it to longitudinally disperse in a radiating undulator. Thus, the method we describe is not applicable for FEL seeding, as the required energy modulations dominate over the FEL bandwidth.

The method, however, is inherently flexible due to the tunability of the laser modulation amplitude. Thus, unlike a facility equipped simply with a short undulator, the length of the pulse train in our scheme can be tailored by adjusting the modulation amplitude. In principle, the length of the pulses achievable is limited only by the energy acceptance limits of the accelerator. In practice however, we observe that space constraints and realistic modulation scenarios may limit achievable modulations to $A \lesssim 0.1$, and thus the cycles to

$N_{\rm cyc} \gtrsim 5$. Nevertheless, it appears possible to produce these few-cycle radiation pulse trains with commercially available undulators and lasers at current facilities.

The coherent radiation process could be further strengthened by using a synthesized waveform in place of a single sine wave. One possibility is to synthesize a triangular or sawtooth waveform by performing the modulation at various harmonics [32]. The resulting bunching regions are more sharply defined, and can possess greater harmonic content as well as a shorter coherent radiation region if issues with the T_{566} transport element and non-sinusoidal modulation can be avoided.

The possibility of a proof of principle experiment at the ATF facility has been presented, in which coherent radiation pulse trains in the 800-1000 nm region could be produced as harmonics of a 10.6μm modulating laser. The analytical theory developed in this paper make no reference to a length scale, and so in principle this method should extend down through the optical, through the UV, and beyond. In principle, however, it may be difficult to create experimentally realizable short-wavelength setups for several reasons. For one, short wavelength radiation generally requires higher energy beams, which require significantly more powerful lasers to achieve modulation amplitudes of a few percent. A good candidate for this modulation might be a high peak power Ti:Sa 800 nm laser, which in a similar configuration to the ATF experiment but with a beam energy of 220 MeV, could produce coherent radiation pulse trains in the 70 nm VUV region. Extension down into the soft X-ray seems possible, but further study is needed to understand if the deleterious effects discussed in section IV incur greater penalties at these short length scales.

ACKNOWLEDGMENTS

L. Campbell and B. McNeil gratefully acknowledge the support of Science and Technology Facilities Council Agreement Number 4163192 Release #3; ARCHIE-WeSt HPC, EPSRC grant EP/K000586/1; EPSRC Grant EP/M011607/1; and John von Neumann Institute for Computing (NIC) on JUROPA at Jlich Supercomputing Centre (JSC), under project HHH20.

Work supported in part by Department of Energy Office of Basic Energy Sciences under Contract DE-AC03-76SF00515.

Appendix A: Off-Axis Field Derivation

To treat off-axis emission in the undulator, we begin with equation (1) and take $\hat{n} = (\sin\theta\cos\phi, \sin\theta\sin\phi, \cos\theta)$ where θ is the angle away from the propagation axis and ϕ is the azimuthal angle. As the particle is assumed ultra-relativistic, we assume $\gamma \gg 1$ and $\theta \ll 1$, keeping terms up to 2nd order in θ and commensurate leading order terms in γ (as the product $\theta\gamma$ may not be small). From the computation of Eq (1) we arrive at,

$$E_x(t') = \frac{4eKk_u\chi^3}{\pi R\epsilon_0}\Big[\gamma^3\left\{-(\theta^2+1)\cos(\omega_u t')(K^2\cos(2\omega_u t') - K^2 + 2)\right\} + \tag{A1}$$
$$\gamma^4\left\{4\theta K\chi\sin(2\omega_u t')\cos(\phi)\left(-K^2\cos(2\omega_u t') + K^2 - 4\right)\right\} +$$
$$\gamma^5\left\{2\theta^2\cos(\omega_u t')\left(-3\left(K^2+2\right)\chi + 3K^2\chi\left(48K^2\chi\sin^4(\omega_u t')\cos^2(\phi) + \sin^2(\omega_u t')\left(-8\left(K^2+2\right)\chi\right.\right.\right.$$
$$\left.\left.\left. + 16K^2\chi\cos^2(\omega_u t')\cos^2(\phi) - 4\left(2\left(K^2+2\right)\chi - 1\right)\cos(2\phi) + 7\right) + \cos^2(\omega_u t')\right) + \cos(2\phi)\right)\right\}\Big]$$

$$E_y(t') = \frac{4eKk_u\chi^3}{\pi R\epsilon_0}\left[\gamma^4\Big\{2\theta K\sin(\phi)\sin(2\omega_u t')\Big\} + \right. \tag{A2}$$
$$\left.\gamma^5\Big\{-2\theta^2\chi\sin(2\phi)\cos(\omega_u t')\left(5K^2\cos(2\omega_u t') - 5K^2 + 2\right)\Big\}\right]$$

$$E_z(t') = \frac{4eKk_u\chi^3}{\pi R\epsilon_0}\Big[\gamma^3\left\{\theta\cos(\phi)\cos(\omega_u t')\left(K^2\cos(2\omega_u t') - K^2 + 2\right)\right\} + \tag{A3}$$
$$\gamma^4\left\{4\theta^2 K\chi\sin(\omega_u t')\cos(\omega_u t')\Big(\frac{1}{2}K^2\Big(-6\sin^2(\omega_u t')\cos(2\phi) + \cos(2\omega_u t') - 3\Big) + \right.$$
$$\left.K^2 + 6\cos^2(\phi) + 2\Big)\right\}\Big]$$

Where we have defined the variable,

$$\chi^{-1} \equiv K^2\cos(2\omega_u t') + K^2 - 2$$

We proceed, as before, by considering only those portions of the field that vary as $\omega_u t'$ and averaging over the rest. The resulting averaged fields are much simplified, and are computed as,

$$\bar{E}_x(t') = \frac{4eKk_u}{\pi R\epsilon_0}\cos(\omega_u t')\Big[\gamma^3(1+\theta^2)\left\{\frac{4+2K^2+K^4}{16(1+K^2)^{5/2}}\right\}\frac{\gamma^5\theta^2}{64(K^2+1)^{7/2}} \tag{A4}$$
$$\left\{\left(3K^8 + 14K^6 + 18K^4 + 96K^2 - 16\right)\cos(2\phi) - 3\left(K^8 + 4K^6 + 6K^4 - 16K^2 + 16\right)\right\}\Big]$$

$$\bar{E}_y(t') = \frac{4eKk_u}{\pi R\epsilon_0}\cos(\omega_u t')\left[\frac{\gamma^5\theta^2\left(K^4 + 8K^2 - 8\right)\sin(\phi)\cos(\phi)}{16\left(K^2+1\right)^{7/2}}\right] \tag{A5}$$

$$\bar{E}_z(t') = \frac{4eKk_u}{\pi R\epsilon_0}\cos(\omega_u t')\left[-\theta\gamma^3\frac{\left(K^4+2K^2+4\right)\cos(\phi)}{16\left(K^2+1\right)^{5/2}}\right] \tag{A6}$$

We note that in the case that $\theta = 0$ we recover the on-axis field result of equation (5). We must also take into account the angle in the relationship between the retarded and observation time, which when averaged over a period, is given by

$$t = \left(1+\frac{K^2}{2}+\gamma^2\theta^2\right)\frac{t'}{2\gamma^2} \tag{A7}$$

The radiation frequency defined in equation (9) thus becomes a function of angle. As before we expand this observation time to first order in the energy deviation $\delta\gamma/\gamma_0$, and arrive at,

$$\omega_u t' = \omega_r(\theta)t\left(1+\frac{2(1+K^2/2)}{1+K^2/2+\gamma_0^2\theta^2}\frac{\delta\gamma}{\gamma_0}\right) \tag{A8}$$

$$\omega_r(\theta) = \frac{2\gamma_0^2}{1+K^2/2+\gamma_0^2\theta^2}\omega_u \tag{A9}$$

Anticipating once again the coherence effect we are interested in, we choose to ignore the amplitude variation caused by relative energy deviation and focus only on this frequency shift. The salient point of difference in comparison to equation (7) is that the factor of 2 in front of the $\delta\gamma/\gamma_0$ has been replaced by,

$$2\frac{1+K^2/2}{1+K^2/2+\gamma_0^2\theta^2} \equiv 2Y(\theta) \tag{A10}$$

Recalling that this factor of 2 also appears in the Bessel function of equation (17), we make the replacement $2 \rightarrow 2Y(\theta)$ to arrive at an angular dependent expression for the resultant x electric field,

$$E_{\mathrm{x,TOT}}^{\mathrm{sin}}(t,\theta,\phi) = N_p E_0(\theta,\phi)\cos\left(\omega_r t\right)J_h\left(2Y(\theta)A\omega_r(\theta)t\right) \tag{A11}$$

Where the factor $E_0(\theta,\phi)$ now contains the γ^3 and γ^5 coefficients of equation (A4). The angular dependence also gives us resultant fields in the y and z direction of analogous form, merely with coefficients taken from equations (A5) and (A6) respectively.

We observe that the effect of the angle θ is to, as in a normal undulator, change the resonant wavelength off-axis. However, through the factor $Y(\theta)$, we now see that different angular components proceed through coherence at different rates. Off-axis radiation components will thus have a slightly longer coherence time, and produce radiation pulses which

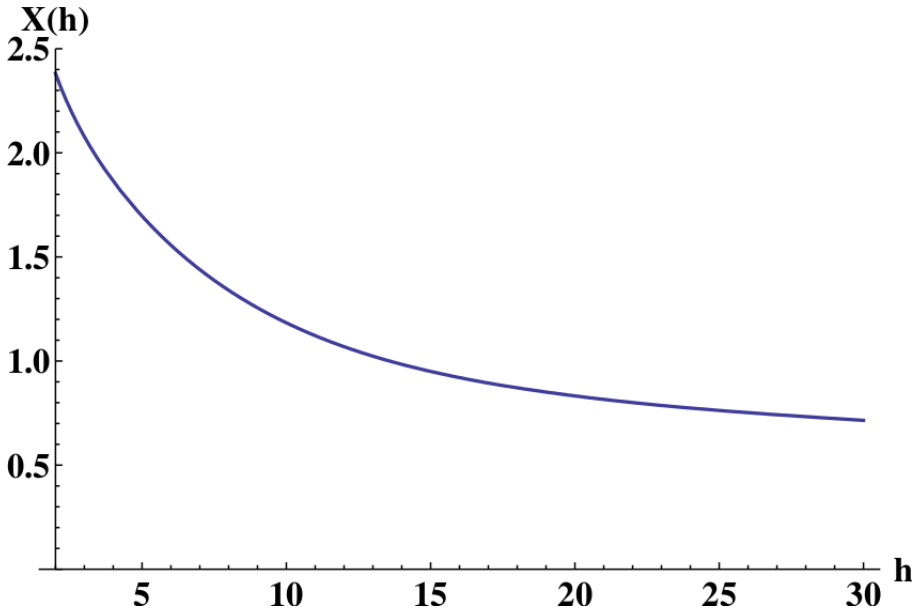

FIG. 10. The universal function $X(h)$ describing how the individual pulse energy varies with harmonic number h.

are spectrally sharper and temporally broader than their on-axis counterparts. This effect can be significant for undulators with relatively small K values at large angles $\theta \sim \gamma^{-1}$, as $Y(\theta = \gamma_0^{-1}) \to 1/2$ for $K \ll 1$, suggesting a doubling of the resultant pulse length compared to the on-axis radiation.

Appendix B: The Universal Function $X(h)$

The universal function $X(h)$ is found by computing the integral from equation (21),

$$\int_0^{t_{\text{final}}} \cos^2(\omega_r t) J_h(2A\omega_r t)^2 dt \tag{B1}$$

where the final emission time $t_{\text{final}} = \frac{1}{2A\omega_r}(2\pi + h)$. The cosine term oscillates quickly compared to the Bessel function, so we approximate it by its average $\langle \cos^2(\omega_r t) \rangle = 1/2$. The relevant integral then becomes,

$$\int_0^{t_{\text{final}}} J_h(2A\omega_r t)^2 dt \tag{B2}$$

This integral can be computed exactly, and it is found to be,

$$\frac{1}{4\sqrt{\pi}A\omega_r}(h+2\pi)^{2h+1}\Gamma\left(h+\frac{1}{2}\right)^2 {}_2\tilde{F}_3\left(h+\frac{1}{2},h+\frac{1}{2};h+1,h+\frac{3}{2},2h+1;-(h+2\pi)^2\right) \tag{B3}$$

where Γ is the Gamma function, and $\tilde{F}$ is a regularized generalized hypergeometric function. The normalization with respect to the standard generalized hypergeometric function is provided by Gamma functions of the second set of arguments: ${}_p\tilde{F}_q\left(a_1\cdots a_p;b_1\cdots b_q;z\right) = {}_pF_q\left(a_1\cdots a_p;b_1\cdots b_q;z\right)/\left(\Gamma(b_1)\cdots\Gamma(b_q)\right)$. The universal function $X(h)$ is then defined as the portion dependent only on h:

$$X(h) = (h+2\pi)^{2h+1}\Gamma\left(h+\frac{1}{2}\right)^2 {}_2\tilde{F}_3\left(h+\frac{1}{2},h+\frac{1}{2};h+1,h+\frac{3}{2},2h+1;-(h+2\pi)^2\right) \tag{B4}$$

The function $X(h)$ turns out to vary only slowly with h, and a plot is shown in Fig. 10. The full result for the individual pulse energy is then given by equation (22).

---

[1] E. Hemsing, G. Stupakov, D. Xiang, and A. Zholents, Rev. Mod. Phys. **86**, 897 (2014).

[2] J. R. Henderson, L. T. Campbell, and B. W. J. McNeil, New Journal of Physics **17**, 083017 (2015).

[3] B. Girard, Y. Lapierre, J. M. Ortega, C. Bazin, M. Billardon, P. Elleaume, M. Bergher, M. Velghe, and Y. Petroff, Phys. Rev. Lett. **53**, 2405 (1984).

[4] G. Stupakov, Phys. Rev. Lett. **102**, 074801 (2009).

[5] L. H. Yu, Phys. Rev. A **44**, 5178 (1991).

[6] D. Xiang and G. Stupakov, Phys. Rev. ST Accel. Beams **12**, 030702 (2009).

[7] Z. Zhao, D. Wang, J. Chen, Z. Chen, H. Deng, J. Ding, C. Feng, Q. Gu, M. Huang, T. Lan, *et al.*, Nature Photonics **6**, 360 (2012).

[8] E. Allaria, R. Appio, L. Badano, W. Barletta, S. Bassanese, S. Biedron, A. Borga, E. Busetto, D. Castronovo, P. Cinquegrana, *et al.*, Nature Photonics **6**, 699 (2012).

[9] E. Allaria, D. Castronovo, P. Cinquegrana, P. Craievich, M. Dal Forno, M. Danailov, G. D'Auria, A. Demidovich, G. De Ninno, S. Di Mitri, *et al.*, Nature Photonics **7**, 913 (2013).

[10] A. A. Zholents and M. S. Zolotorev, Phys. Rev. Lett. **76**, 912 (1996).

[11] R. W. Schoenlein, S. Chattopadhyay, H. H. W. Chong, T. E. Glover, P. A. Heimann, C. V. Shank, A. A. Zholents, and M. S. Zolotorev, Science **287**, 2237 (2000).

[12] A. A. Zholents and W. M. Fawley, Phys. Rev. Lett. **92**, 224801 (2004).

[13] N. R. Thompson and B. W. J. McNeil, Phys. Rev. Lett. **100**, 203901 (2008).

[14] D. Xiang, Y. Ding, T. Raubenheimer, and J. Wu, Phys. Rev. ST Accel. Beams **15**, 050707 (2012).

[15] B. W. J. McNeil, N. R. Thompson, D. J. Dunning, and B. Sheehy, Journal of Physics B: Atomic, Molecular and Optical Physics **44**, 065404 (2011).

[16] D. Hai-Xiao and D. Zhi-Min, Chinese Physics C **34**, 1140 (2010).

[17] A. Hofmann, *The physics of synchrotron radiation*, Vol. 20 (Cambridge University Press, 2004).

[18] L. Campbell and B. McNeil, in *Proceedings of the 2012 FEL Conference* (Nara, Japan, 2012) pp. 626–629.

[19] DLMF, "NIST Digital Library of Mathematical Functions," http://dlmf.nist.gov/10.21.E40, Release 1.0.10 of 2015-08-07.

[20] L. T. Campbell and B. W. J. McNeil, Physics of Plasmas **19**, 093119 (2012), http://dx.doi.org/10.1063/1.4752743.

[21] R. Carr, M. Cornacchia, P. Emma, H.-D. e. Nuhn, B. Poling, R. Ruland, E. Johnson, J. Rakowsky, George an d Skaritka, S. Lidia, P. Duffy, M. Libkind, P. Frigolã, A. Murokh, C. Pellegrini, J. Rosenzweig, and A. Tremaine, Phys. Rev. ST Accel. Beams **4**, 122402 (2001).

[22] E. D. Courant, C. Pellegrini, and W. Zakowicz, Phys. Rev. A **32**, 2813 (1985).

[23] S.-Y. Lee, *Accelerator physics* (World Scientific Publishing Co Inc, 2004).

[24] A. A. Zholents, Phys. Rev. ST Accel. Beams **8**, 040701 (2005).

[25] M. E. Jones and B. E. Carlsten, in *Proceedings of the Particle Accelerator Conference, 1987* (1987) p. 1319.

[26] M. Reiser, *Theory and Design of Charged Particle Beams* (Wiley-VCH, 2008).

[27] M. Venturini, Phys. Rev. ST Accel. Beams **11**, 034401 (2008).

[28] W. D. Kimura, L. P. Campbell, C. E. Dilley, S. C. Gottschalk, D. C. Quimby, M. Babzien, I. Ben-Zvi, J. C. Gallardo, K. P. Kusche, I. V. Pogorelsky, J. Skaritka, V. Yakimenko, F. Zhou, D. B. Cline, L. C. Steinhauer, and R. H. Pantell, in *Proceedings of the Particle Accelerator Conference, 2003.* (2003) pp. 1909–1911 vol.3.

[29] P. M. Paul, E. S. Toma, P. Breger, G. Mullot, F. Augé, P. Balcou, H. G. Muller, and

P. Agostini, Science **292**, 1689 (2001).

[30] T. Popmintchev, M.-C. Chen, A. Bahabad, M. Gerrity, P. Sidorenko, O. Cohen, I. P. Christov, M. M. Murnane, and H. C. Kapteyn, Proceedings of the National Academy of Sciences **106**, 10516 (2009).

[31] G. Sansone, L. Poletto, and M. Nisoli, Nature Photonics **5**, 655 (2011).

[32] E. Hemsing and D. Xiang, Phys. Rev. ST Accel. Beams **16**, 010706 (2013).